Biosensors and Bioelectronics 178 (2021) 113038

Contents lists available at ScienceDirect

Biosensors and Bioelectronics

journal homepage: http://www.elsevier.com/locate/bios

Biological small-molecule assays using gradient-based microfluidics

Morteza Azizi [a], Benyamin Davaji [b], Ann V. Nguyen [a], Amir Mokhtare [a], Shiying Zhang [c], Belgin Dogan [c], Patrick A. Gibney [a], Kenneth W. Simpson [c], Alireza Abbaspourrad [a,*]

[a] Department of Food Science, College of Agricultural and Life Sciences, Cornell University, Stocking Hall, Ithaca, NY, 14853, USA
[b] School of Electrical and Computer Engineering, Cornell University, Philips Hall, Ithaca, NY, 14853, USA
[c] Department of Clinical Sciences, College of Veterinary Medicine, Cornell University, 602 Tower Rd., Ithaca, NY, 14853, USA

ARTICLE INFO

Keywords:
Microfluidics
Biosensors
Biological small-molecule
High-throughput biosensing
Antimicrobial susceptibility testing

ABSTRACT

Studying the potency of small-molecules on eukaryotic and prokaryotic cells using conventional biological settings requires time-consuming procedures and large volumes of expensive small-molecules. Microfluidics could significantly expedite these assays by enabling operation in high-throughput and (semi)automated modes. Here, we introduce a microfluidics platform based on multi-volume microchamber arrays that can produce a wide range of small-molecule concentrations with a desired gradient-based profile for rapid and precise biological testing within a single device with minimal hands-on time. The concept behind this device is based on introducing the same amount of a small-molecule into microchambers of different volumes to spontaneously generate a gradient concentration profile *via* diffusion. This design enables to obtain an unprecedented concentration range (*e.g.*, three orders of magnitude) that can be easily adjusted, allowing us to pinpoint the precise effect of small-molecules on pre-loaded prokaryotic and eukaryotic cells. We also propose a comprehensive relationship for determining the loading time (the only required parameter for implementing this platform) in order to study the effects of any small-molecule on a biological species in a desired test. We demonstrate the versatility of this microfluidics platform by conducting two small-molecule assays—antimicrobial resistance and sugar-phosphate toxicity for both eukaryotic and prokaryotic biological systems.

1. Introduction

To decipher the functions and side-effects between an organic small-molecule (approximately < 900 Daltons) and a biological species (live eukaryotic and prokaryotic cells), conventional biological assays often use 96 well-plates, in which each well is used to test a different small-molecule concentration (Alsenaid et al., 2020; Mosquera et al., 2018; Sarzi-Puttini et al., 2019). However, sample preparation is time-consuming, costly, and labor-intensive, often requiring large reagent volumes (Lamb et al., 2006; Stockwell 2004). To address these issues, robotics can shorten assay times (Reddy et al., 2018; Wootton and deMello 2012). However, such systems are generally bulky and expensive, which can impede their use in biological applications, particularly in resource-limited settings (Huang et al., 2018; Liu et al., 2019; Xu et al., 2018a).

As an alternative, miniaturization of biological assays using microfluidics may be an ideal solution for improving throughput and lowering costs (Avesar et al., 2017; Azizi et al., 2018; Baltekin et al., 2017; Campbell et al., 2016; Hong et al., 2018; Kao et al., 2020; Kim et al., 2019; Li et al., 2019; Mohan et al., 2013; Yang et al., 2020). Small-molecule concentration-based biological assays can be performed in microfluidic systems with significantly improved precision (Leonard et al., 2017; Li et al., 2019; Syal et al., 2016). For example, one of the most studied platforms for this application uses a well-known "Christmas tree" technique (Jang et al., 2011; Kim et al., 2012; Lim and Park 2018). Although, Christmas tree technique produces precise concentrations of a drug in a microfluidic chip, however, it needs precision instruments (such as syringe pumps) to robustly control the flowrates of two loading fluids. Moreover, such designs require time-consuming sample-loading protocols that cannot be easily automated, and more importantly, lack enough throughput to enable simultaneous testing of negative controls and a wide concentration range of positive samples in a single test.

To overcome these limitations, we propose a novel multi-volume microchamber-based microfluidic (MVM^2) platform that is designed to produce a spontaneous and broad gradient of small-molecule

* Corresponding author.
E-mail address: Alireza@cornell.edu (A. Abbaspourrad).

https://doi.org/10.1016/j.bios.2021.113038
Received 13 August 2020; Received in revised form 18 January 2021; Accepted 23 January 2021
Available online 27 January 2021

concentrations within a single test. Antibiotic susceptibility testing and sugar phosphate toxicity (Gibney et al., 2018; Johnston and Strobel 2019; Machado et al., 2017; Xu et al., 2018b) (for bacteria and yeast cells, respectively) are studied as two clinical models to demonstrate the versatility of the MVM^2 platform. We also obtain the loading time—as the only parameter needed to be controlled by a simple operator for running the MVM^2 platform—for a wide-range of commercial biological small-molecules in the market including anticancer drugs, antibiotics, and antifungals. Overall, with the MVM^2 design, we can rapidly determine precise effects of small-molecules in a broad concentration range with high throughput and low cost, and in a manner that is readily adaptable for automation.

2. Material and methods

2.1. Materials

We obtained SU-8 (2050) negative photoresist and its developer from Microchem Corp. (Newton, MA). The silicon wafer (ID: 452) was purchased from UniversityWafer (Boston, MA). For device fabrication, polydimethylsiloxane (PDMS, Sylgard 184) and its curing agent were purchased from Dow Corning (Albany, NY). Moreover, polyethylene tubing (Interior diameter = 0.38 mm, outside diameter = 1.09 mm), 27–gauge syringe needles, and 3 mL Luer–Lok tip disposable syringes were purchased from Becton Dickinson (Rockville, MD). Cellophane tape was purchased from 3M (Scotch Magic, USA).

We purchased all antibiotics, including kanamycin, ampicillin, gentamicin, nalidixic acid, lincomycin, cefuroxime, from Sigma Aldrich (St. Louis, MO). The *in vitro* toxicology assay kit, PrestoBlue™ Cell Viability Reagent was purchased from Thermo Fisher scientific (San Jose, CA). Non-selective Difco™ Mueller Hinton (MH) broth and selective Lysogeny Broth (LB) culture media were obtained from Becton Dickinson Co. (Rockville, MD) and ThermoFisher Scientific (San Jose, CA), respectively. For the broth microdilution test, 96 MicroWell plates were purchased from Becton Dickinson Falcon (Rockville, MD).

2.2. MVM^2 device fabrication

We followed the Microchem Corp. (MA, USA) instruction for microfluidic device fabrication using the well-established soft lithography technique (and and Whitesides 1998; Pajoumshariati et al., 2018a; Pajoumshariati et al., 2018b; Yaghoobi et al., 2020). Briefly, SU-8 2050 was poured on a silicon wafer and spun-coated at 2100 rpm. Then, it was pre-baked at 65 °C and 95 °C for 3 and 9 min, respectively. The pre-baked SU-8 photoresist was then patterned using a photomask made by CAD/Art Services, Inc. (Bandon, OR) *via* UV light wavelength with an exposure energy of 120 mJ/cm^2 at 365 nm. Then, a post-baking step was followed at 65 °C and 95 °C for 2 and 7 min, respectively, to further permanently stabilize the SU-8 photoresist pattern on the silicon wafer. We then developed and washed the uncured SU-8 (non-patterned parts of SU-8) by gently soaking the SU-8 patterned silicon wafer in the SU-8 developer for 10 min.

2.3. Bacteria culture medium, strains, growth, and broth microdilution test

We used non-selective MH culture medium for all bacterial culture. In detail, a colony of bacteria pre-cultured on an LB agar plate (Corning, NY) was taken from a freshly streaked plate and suspended into 3 mL of MH broth, and cultured at 37 °C overnight (~12 h). The concentration of bacterial suspension was adjusted using a UV–vis spectrophotometer (Thermo Fisher Scientific-brand NanoDrop macchine; Wilmington, DE). To do this, the overnight culture medium was diluted by 10-fold serial dilutions in non-selective MH culture medium to find the appropriate final concentration (1×10^6 CFU/mL) for the antimicrobial susceptibility testing assay.

2.4. Yeast culture medium, strains, and growth

All media used was either minimal medium (YNB; 0.67% yeast nitrogen base without amino acids plus 2% indicated carbon sources) or rich medium (YP; 2% bacto peptone, 1% yeast extract, 2% indicated carbon sources). Additionally, for fluorescence microscopy, low-fluorescence medium was used (standard minimal medium with 2% glucose, except YNB is prepared without riboflavin or folic acid to reduce background fluorescence) (Sheff and Thorn, 2004). The yeast strains used in this study are listed in Table 1. DBY12000 yeast strain is the wild-type yeast strain (*i.e.*, WT) while the other strain—*i.e.*, DBY12549 or yrKHK—is the mutant of the wild-type yeast strain, which is sensitive to fructose.

2.5. Antimicrobial testing (gold standard broth microdilution test)

The gold standard broth microdilution test (Wikler et al., 2012) was performed by preparing the antibiotic solutions at their final concentrations from a stock solution of each examined antibiotic. A fresh 200 μL volume of each antibiotic solution (prepared in MH culture medium) was pipetted into each microwell of a 96 MicroWell plate. Note, the concentrations of each antibiotic solution was set at 0.1–1 μg/mL (by 0.1 μg/mL-unit increment between every two consecutive antibiotic concentrations), 1–10 μg/mL (by 1 μg/mL-unit increment between every two consecutive antibiotic concentrations) and 10–100 μg/mL (by 10 μg/mL-unit increment between every two consecutive antibiotic concentrations). Then, 10 μL of each bacterial stock suspension was added to each microwell containing antibiotic solution to reach the appropriate bacterial final concentration (1×10^6 CFU/mL). We incubated the bacteria in the presence of antibiotics for 20 h, and then measured the MIC and antimicrobial resistant assay time upon 80% reduction in the OD_{600}–growth curves compared to the negative control (*i.e.*, without adding any antibiotic to the bacterial suspension). Bacteria were grown at 37 °C shaking for 24 h. Standardized growth curve analysis was performed using a Bioscreen C automated plate reader (Growth Curves USA, NJ) by measuring OD_{600}. All experiments were completed in triplicate and performed twice.

2.6. Computational fluid dynamics (CFD) simulations

COMSOL Multiphysics (version 5.3; COMSOL Inc., USA) was used to carry out to obtain the flow velocities and concentration profiles. 2D creeping flow module was used as the flow and boundary condition were considered as: (i) boundary condition: pressure 0 Pa; (ii) wall condition: no slip; (iii) considering the suppression of backflow; and (iv) normal physics-controlled for mesh size. We solved the Navier-Stokes (Eq. (1)) and conservation of mass (Eq. (2)) equations:

$$\rho(V.\nabla V) = -\nabla P + \nabla.\mu\left(\nabla V + (\nabla V)^T\right) \quad (1)$$

$$\nabla.V = 0 \quad (2)$$

in which V denotes the velocity field, ρ is the density of the culture medium, P is pressure, and μ is the dynamic viscosity.

2.7. Small-molecule diffusion coefficient determination

Based on the spectrophotometry method, 4 mL culture medium was loaded into a cuvette, followed by 80 μL of antibiotics (*e.g.*, nalidixic

Table 1
Yeast strains used for sugar phosphate toxicity study in the MVM2 platform.

Strain	Name in the text	Genotype
DBY12000	WT	MAT**a** prototrophic HAP1$^+$ derivative of FY4
DBY12549	yrKHK	MAT**a** HAP1$^+$ can1Δ::TDH3$_{pr}$-yrKHK

acid, ampicillin, and cefuroxime plus resazurin as a fluorescent chemical; initial concentration = 10 mg/mL) that was gently loaded at the bottom of the cuvette using a chromatography syringe. The diffusion kinetics of the antibiotics were obtained from the UV absorbance of their maximum wavelengths (correlated with concentration) as they diffused up through the cuvette over time.

2.8. '$D_1 \times t_1 = D_2 \times t_2$' derivation

To empirically determine the diffusion coefficients of the antibiotics in culture media, we measured the UV absorbance spectrum of the antibiotics diffusing up in a cuvette. These values (*i.e.*, UV absorbance data-points) can be correlated with a mathematical equation. To obtain the theoretical model of mass transport in the cuvette, the mass transfer was considered in a Cartesian geometry due to the rectangular cuboid shape of the cuvette (Fig. 3d in the main manuscript). To simplify the equation, the mass transport was assumed to be one-dimensional ('y' direction: the cuvette height direction). Moreover, the antibiotic diffusion into the culture medium was considered as an unsteady-state phenomenon, as represented in Eq. (3).

$$\frac{\partial C(y,t)}{\partial t} = D\frac{\partial^2 C(y,t)}{\partial y^2} \tag{3}$$

in which, C, t, and D denote the antibiotic concentration, time, and diffusion coefficient, respectively.

By substituting t × D with as a variable (and $tD = t'$, consequently) into Eq. (4), it can be simplified to Eq. (4):

$$\frac{\partial C(y,t')}{\partial t'} = \frac{\partial^2 C(y,t')}{\partial y^2} \tag{4}$$

Two insulated boundary conditions were considered in the 'y' direction (the top and bottom layers of solution in the cuvette). The boundary conditions and the initial conditions were considered as follows (Eqs. (5) and (6)):

$$\frac{\partial C(0,t)}{\partial t} = 0 \Rightarrow \frac{\partial C(0,t')}{\partial t} = 0 \tag{5}$$

$$\frac{\partial C(L,t)}{\partial t} = 0 \Rightarrow \frac{\partial C(L,t)}{\partial t} = 0 \tag{6}$$

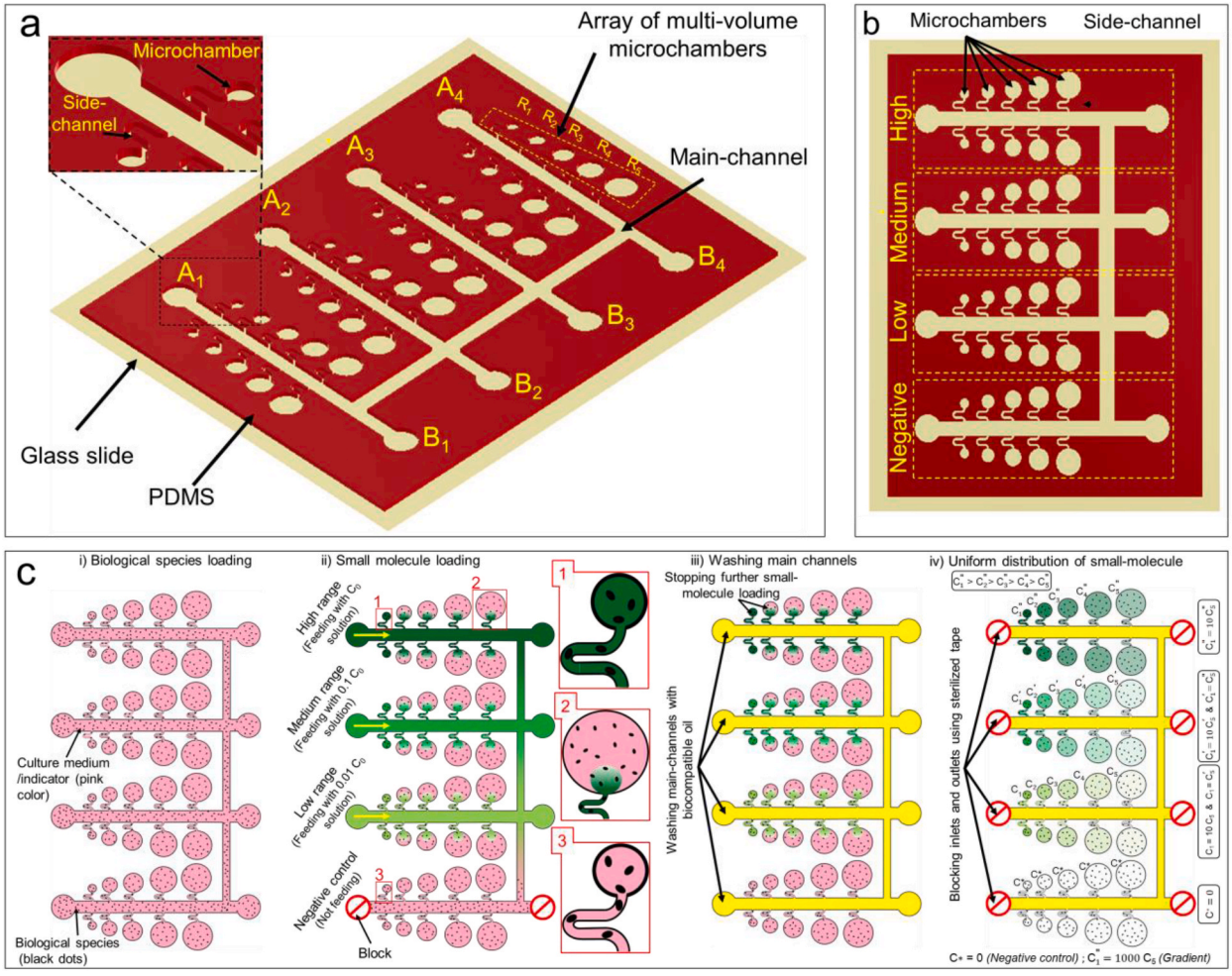

Fig. 1. MVM^2 features and sample loading principles. (a) Schematic structure of the MVM^2 platform, in which only microchambers R_1–R_5 are shown for simplicity. (inset) Schematic illustration of a microchamber connected to the main channel. (b) The features of the MVM^2 platform, demonstrating the design of the negative, low, medium, and high concentration small-molecule main-channels. (c) The assay loading steps, including: (i) biological species loading (uniform concentration throughout); (ii) small-molecule loading into the positive main-channels by diffusion at three orders of magnitude (C_0, 0.1 C_0, and 0.01 C_0); (iii) stopping the loading of the small-molecules by washing the main-channels with a biocompatible oil to isolate the microchambers containing the biological species and small-molecules; and (iv) blocking the inlets and outlets with sterilized medical tape and letting the loaded small-molecules uniformly distribute in the microchambers. As a result, the smallest (R_1) and largest (R_{12}) microchambers in each row feature the highest and lowest concentrations of the small-molecule in the low, medium, and high ranges. Moreover, the smallest microchambers of the low and medium ranges feature identical concentrations as the largest microchambers of the medium and high ranges, respectively, ensuring there is continuity within the concentrations tested.

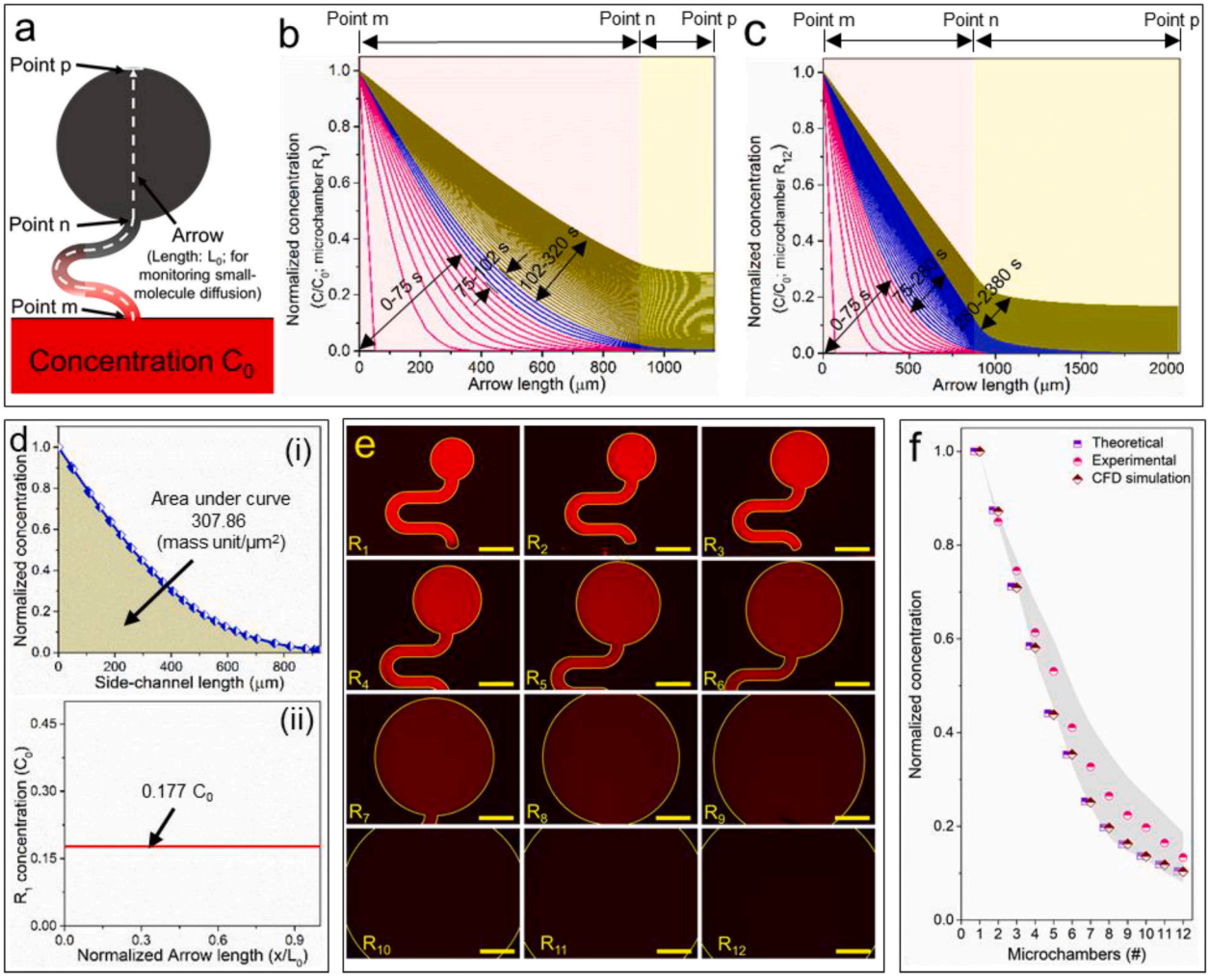

Fig. 2. Characterization of resazurin loading in the MVM^2 platform. (a) The dashed schematic arrow (length L_0) for monitoring the resazurin diffusion into the microchamber, with three points designated (m, n, and p), representing the starting point of the side-channel inlet, the junction where the inlet connects to the microchamber, and the farthest point in the microchamber from the side-channel inlet, respectively. (b, c) Resazurin concentration profiles determined by CFD simulations for microchambers R_1 and R_{12}, respectively. We chose microchambers R_1 and R_{12} to study the kinetics of resazurin diffusion as the diffusion trend can be generalized for the 10 remaining microchambers, R_2–R_{11}, which are of intervening size. (d) Before (i) and after (ii) the uniform distribution of resazurin into the side-channel and the corresponding microchamber R_1. (e) The experimentally observed GCP of resazurin loading in microchambers R_1–R_{12}. (f) Comparing the normalized GCPs obtained by experimental (n = 5) and CFD simulation of resazurin with the theoretical data (obtained from the microchambers' volumes and normalization of the small-molecule concentrations). Scale-bar: 200 μm. The shaded gray area corresponds to the error bars.

We used two first terms of the Taylor series as initial conditions, as follows:

$$\exp(-x2) = 1 - x^2 + \frac{x^2}{4} - \frac{x^6}{6} + \frac{x^8}{24} + \ldots \tag{7}$$

Using the "Separation of Variables" method, the answer for Eq. (8) can be defined as follows:

$$C(y,t') = Y(y).T(t) \tag{8}$$

Plugging Eq. (8) into Eq. (4) leads to the following equation:

$$T'.Y = Y''.T \Rightarrow \frac{T'}{T} = \frac{Y''}{Y} = \lambda = -k^2 = constant \tag{9}$$

Eq. (9) can be solved and simplified by using the boundary conditions.

$$\frac{C}{C_0}(Y,t') = \sum_{n=0}^{\infty} a_n.exp^{\frac{-n^2\pi^2}{L^2}t'} \cos\left(\frac{n\pi}{L}Y\right) \tag{10}$$

Substituting $tD = t'$ into Eq. (10) leads to:

$$\frac{C}{C_0}(y,t) = \sum_{n=0}^{\infty} a_n.exp^{\frac{-n^2\pi^2}{L^2}Dt}.\cos\left(\frac{n\pi}{L}y\right) \tag{11}$$

Using the initial condition to find a_n results in Eq. (12):

$$\frac{C}{C_0}(y,t) = \frac{4}{3} + \frac{2L^3}{\pi^3}\sum_{n=1}^{\infty}\frac{(-2)(-1)^{n+1}}{n^2}.exp^{\frac{-n^2\pi^2}{L^2}Dt}.\cos\left(\frac{n\pi}{L}y\right) \tag{12}$$

For $n \gg 2$, the terms of series were negligible. Then, we used the two first sentences of Eq. (12) which led to Eq. (11). The empirical data obtained with UV–vis spectrophotometry was correlated with Eq. (11) and the diffusion coefficient for each antibiotic was then calculated:

$$\frac{C}{C_0}(y,t) = \frac{4}{3} + \frac{2L^3}{\pi^3}\left(2.exp^{\frac{-\pi^2}{L^2}Dt}.\cos\left(\frac{\pi}{L}\right)y - \frac{1}{2}exp^{\frac{-4\pi^2}{L^2}Dt}.\cos\left(\frac{2\pi}{L}\right)y\right) \tag{13}$$

2.9. Imaging platform

ZOE™ fluorescent cell imager (Bio-Rad, CA) was used as an imaging

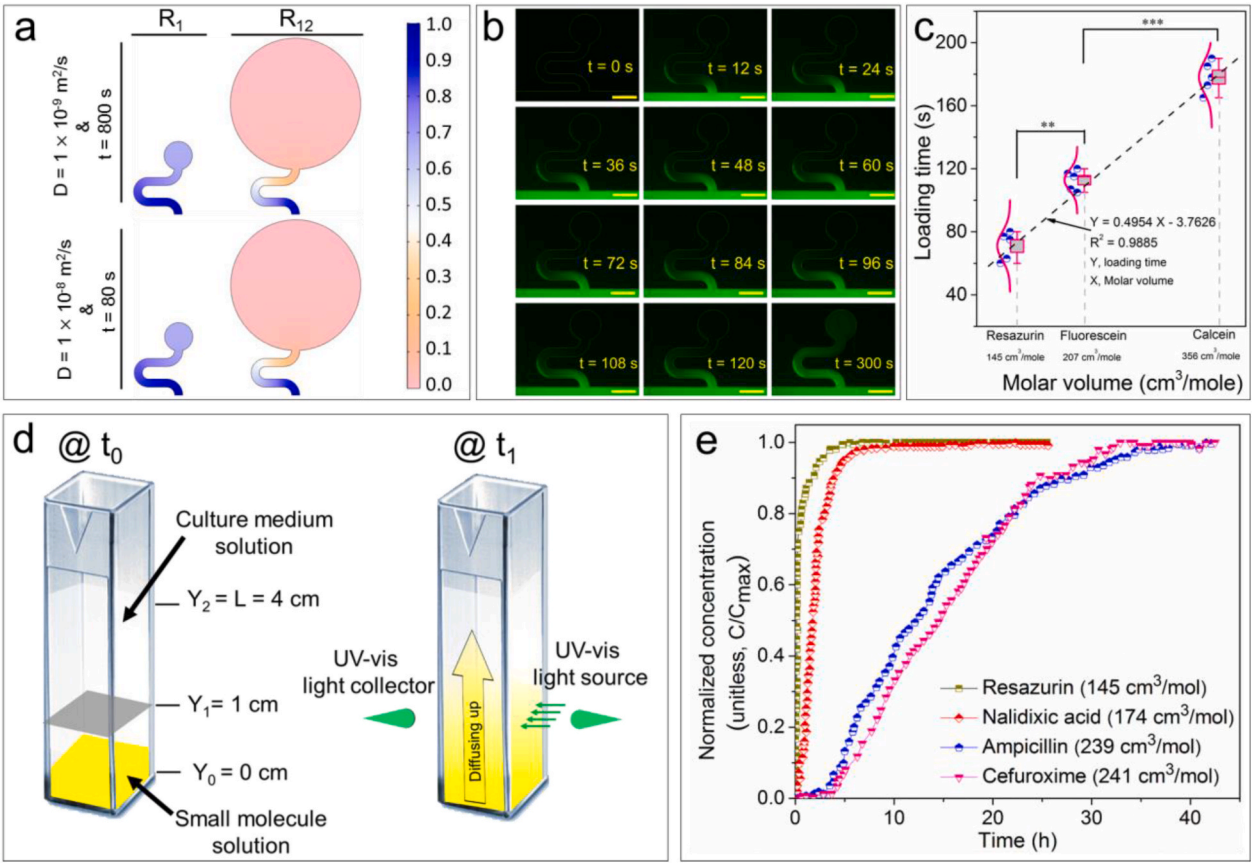

Fig. 3. Correlation between the small-molecule molar volume and loading time in the MVM^2 platform. (a) CFD simulations for microchambers R_1 and R_{12} confirm the relationship between the diffusion coefficients and loading times of any two small-molecules, satisfying the equation $D_1 \times t_1 = D_2 \times t_2$. The CFD simulations show identical concentration profiles (i.e., same color patterns) for two small-molecules with different loading times, satisfying the relationship $D_1 \times t_1 = D_2 \times t_2$. (b) Time-lapse calcein diffusion into microchamber R_1. The fluorescent calcein gradually diffuses into the side-channel and the connected microchamber over the loading time. Scale-bar: 200 μm. (c) Validation of the relationship $Molar\ volume_1 \times t_2 = Molar\ volume_2 \times t_1$ between the loading times and their molar volumes, tested for three fluorescent dyes—resazurin, fluorescein, and calcein. The obtained trend-line fit of the loading times for resazurin, fluorescein, and calcein is described by $Loading\ time = 0.4954 \times molar\ volume - 3.7623$, with $R^2 = 0.9885$. This equation can be used to obtain the loading times for other small-molecules applicable in the MVM^2 platform (** and ***: p values < 0.01 and 0.001, respectively). (d) A technique for testing the correlation between the small-molecule diffusion coefficients and molar volumes. The small-molecule solution is gently loaded at the bottom of a cuvette using a chromatography syringe. (e) Normalized concentration versus diffusion time for four tested small molecules, including ampicillin, cefuroxime, resazurin, and nalidixic acid. (For interpretation of the references to color in this figure legend, the reader is referred to the Web version of this article.)

platform to take the images of the microchambers, and ImageJ software was utilized to convert the fluorescent intensity to gray value.

2.10. Data analysis

The fluorescence of the medium within the wells was calculated by averaging the pixel intensities in a given semi–spherical region. A custom MATLAB script was used to analyze the images.

3. Results and discussion

3.1. MVM^2 device compartments and operational protocol

The MVM^2 platform features four main-channels in parallel, with openings at the ends of each main-channel (*i.e.*, A_1–A_4 and B_1–B_4; Fig. 1a). Moreover, arrays of dead-end microchambers, each containing a different volume increasing in size from R_1 to R_{12}, are connected to each side of the main-channels *via* identical side-channels (Fig. 1a and Fig. S1). Fig. 1b shows how the biological assay design is integrated with the MVM^2 platform, in which the microchambers connected to one of the main channels is reserved for the 'negative control' test (*i.e.*, no small-molecule exposure), while the remaining three channels provide the positive low, medium, and high concentration ranges of the small-molecule at three orders of magnitude (*e.g.*, 0.1–1, 1–10, and 10–100 μg/mL for the low, medium, and high ranges, respectively).

To perform a small-molecule-based biological assay in the MVM^2 platform, we follow four main steps to load the reagents. Step-i involves loading a suspension of the biological species (often with a fluorescent chemical indicator) into the MVM^2 platform so that it is uniformly distributed throughout (Fig. 1ci and Fig. S2 for more details; this step mainly takes ~ 3–5 min). In step-ii, we load small-molecule solutions at C_0, 0.1 C_0, and 0.01 C_0 concentrations into the high, medium, and low positive main-channels, respectively, which diffuse into the corresponding microchambers through the connected side-channels (Fig. 1cii and Fig. S3 for more details; this step mainly takes as equal as the small-molecule loading time). To obtain a controllable and rational small-molecule loading time, we designed the serpentine-like side-channels (Fig. S4).

Importantly, there are two potential scenarios to make a gradient-based concentration profile (GCP) of the small-molecules in a platform: (a) exposing different amounts of a small-molecule with the same number of a biological species, or (b) exposing the same amount of a small-molecule with different numbers of a biological species. We chose the second method in MVM^2 platform as it requires exposing the same

amounts of a small-molecule (*i.e.*, identical green-color patterns in microchambers of the low, medium, or high range as shown in Fig. 1cii) with different number of biological species, as loaded into multi-volume microchambers R_1–R_{12} (note that the volume of R_{12} is 10-times larger than R_1). This results in distinct C_1–C_{12} concentrations within each low, medium, and high ranges.

We achieve such a GCP in step-ii of the loading process by subsequently washing the main-channels with a biocompatible oil to stop further small-molecule loading and isolate the microchambers avoiding any chemical exchange between adjacent microchambers (it takes ~ 5–10 s). In step-iv (Fig. 1civ), we allow these small molecules to uniformly diffuse and distribute within each isolated microchamber, producing a GCP in each microchamber array. This MVM^2 design helps us to investigate the effects of dozens of small-molecule concentrations on a biological species, enabling important biological effects to be rapidly pinpointed in a single test (*e.g.*, susceptibility or resistance of a biological species to a small-molecule drug, as schematically shown in Fig. S5).

3.2. MVM^2 platform characterization for a typical small-molecule

To validate our hypothesis of small-molecule loading into the multi-volume microchambers *via* diffusion in the MVM^2 platform, we used a 20% wt/v solution of resazurin (a fluorescent small-molecule). We then monitored the resazurin diffusion through a preloaded aqueous phase (Mueller-Hinton culture medium) and found that resazurin successfully moved through the side-channel and entered the microchamber (Fig. S6). Computational fluid dynamics (CFD) simulation of this process also demonstrated the formation of dead-zones in the microchambers and side-channels (Fig. S7). This indicates the small molecules are driven into the microchambers by a diffusion mechanism alone (*i.e.*, no mass transport through convention).

Control over the small-molecule diffusion into the microchambers is pivotal for obtaining a GCP, which is governed by the loading time (defines as the time period between loading the small molecule into the main channels and flushing the system with oil). For an unlimited loading time (∞), the microchambers become fully saturated, leading to the failure of GCP formation (Fig. S8). Therefore, to find the optimum loading time for resazurin, we monitored its diffusion by measuring the position of the fluorescent solution along the side-channel and microchamber, as schematically shown by the white dashed arrow marked at positions 'm,' 'n,' and 'p' in Fig. 2a.

We obtained the CFD-based time-dependent normalized concentration profiles—divided by the maximum concentration, C_0—along the dashed arrow for microchambers R_1 (smallest) and R_{12} (largest) (Fig. 2b and c). As shown in Fig. 2b and c, the kinetics of resazurin loading follows three phases before the small-molecule fully saturates the aqueous medium in the microchambers (*i.e.*, a normalized concentration of 1). In phase-i, the resazurin solution loaded into the main channel (normalized concentration of 1) moves along the side-channel—from point m to point n—within 75 s (pink curves in Fig. 2b and c). In phase-ii, more resazurin diffuses into the side-channels and microchambers, eventually reaching point p (blue curves in Fig. 2b and c). Finally, even more resazurin diffuses and the concentration of every position along the dashed arrow increases, culminating in saturation of the features (phase-ii; dark yellow curves in Fig. 2b and c).

To investigate the criterion for achieving resazurin GCP in the MVM^2 platform (*i.e.*, loading the same amount of resazurin into the multi-volume microchambers at a specific time-point), we chose the concentration profile at t = 75 s (pink curve, Fig. 2b and c) as only the first phase (diffusion through the side-channels) was the same for all microchambers R_1–R_{12}. The concentration profiles at t = 75 s (after washing off with the biocompatible oil) and $t \gg 75$ s (shown in Fig. 2di and 2dii, respectively) demonstrate the before and after the uniform distribution of the small-molecule concentration in the side-channel and corresponding microchamber R_1. We calculated the area under the curve before uniform distribution (Fig. 2di), which represents the net amount of resazurin (307.86 mass unit/μm^2) loaded into just microchamber R_1's side-channel. This would result in microchamber R_1 obtaining a uniform resazurin concentration profile of 0.177 C_0 after the even distribution of resazurin into both the side-channel and its connected microchamber R_1 (Fig. 2dii). Meanwhile microchamber R_{12}, which features 10-times larger volume than R_1, would feature a 10-times lower concentration (0.0177 C_0), while the remaining multi-volume microchambers (R_2–R_{11}) achieve an intervening range of concentrations ($0.177\ C_0 < C < 0.0177\ C_0$), resulting in the successful formation of a GCP. Logically, there are different time periods for microchambers with different sizes (R_1–R_{12}) to obtain uniform small-molecule drug distribution. The largest microchamber (R_{12}) requires the longest time to have the small-molecule drug fully distributed into it. Therefore, we perform CFD simulations for the microchamber R_{12} to find out how long it takes for a small-molecule such as resazurin to be uniformly distributed (Fig. S9).

We used the time-point found by CFD simulations (t = 75 s) to experimentally verify that resazurin can achieve a GCP in our MVM^2 setup. After loading the resazurin into microchambers R_1–R_{12} for 75 s (as the loading time), we found the fluorescence of the microchambers decreases with increasing microchamber size, indicating a successful GCP (Fig. 2e). We designed the microchamber and consequently, know the volume of all microchambers. This helps us to find the concentrations of microchambers theoretically, if hypothetically the same amounts of small-molecules is loaded into microchambers R_1–R_{12}. Upon normalization of microchambers' concentrations using Eq. (14), we calculate the theoretical normalized concentrations of all microchambers to compare with the experimental ones (Fig. 2h).

$$Normalized\ concentration_{microchamber_{Ri}} = \frac{Volume_{microchamber_{R1}}}{Volume_{microchamber_{Ri}}} \tag{14}$$

Fig. 2f confirms good agreement between the normalized GCPs obtained by experimental and CFD simulation approaches with the theoretical GCP (obtained using Eq. (14)).

3.3. Versatility of the MVM^2 platform for biological small-molecules

The diffusion of small-molecules into the multi-volume microchambers is the key for producing a GCP. However, it is well-known that small-molecules have different diffusion coefficients, which is most impacted by their molecular size. As a result, loading small-molecules with different diffusion coefficients at the same loading time could result in different GCPs in the MVM^2 platform, as shown in Fig. S10a–c, S11 and S12. Using an analytical solution for small-molecule mass transport in the side-channels and microchambers (see Supplementary Information, part 1.8.) and CFD simulations for microchambers R_1 and R_{12} (Fig. 3a and Fig. S13), we found that the loading time (t) and diffusion coefficients (D) for any two small-molecules follow the relationship $D_1 \times t_1 = D_2 \times t_2$. This relationship can help us to determine the loading time (*e.g.*, t_2) for achieving a GCP for any biological small-molecule based on the loading time and diffusion coefficient of a known small-molecule (*e.g.*, resazurin with t_1 = 75 s and $D_1 = 1.06 \times 10^{-6} \frac{cm^2}{s}$) as well as the diffusion coefficient of the target small-molecule (*e.g.*, D_2).

However, there is no extensive database available for the diffusion coefficients of biological small-molecules. Therefore, we instead chose the small molecule's molar volume to investigate its relationship with the loading time, as the molar volume is more readily accessible compared to the diffusion coefficient. Toward this aim, we studied the loading kinetics of different fluorescent dyes, including calcein (Fig. 3b), fluorescein (Fig. S14), and resazurin (Fig. S6a) in the R_1 side-channel and microchamber. Note, the molar volumes of calcein, fluorescein, and resazurin are 356 ± 5 cm^3/mol, 208 ± 4, and 145 ± 7, respectively. Interrogating the loading kinetics of the fluorescent dyes into the side-channel helped us to find a linear relationship between the small-

molecules' molar volumes and loading times (R^2 = 0.9885) in the MVM^2 platform, as follows (Fig. S10d and Fig. 3c).

$$Loading\ time = 0.4954 \times molar\ volume - 3.7623 \quad \text{Eq. 15}$$

To further confirm that Eq. (15) can also apply to non-fluorescent biological small-molecules, we employed a simple method using spectrophotometry. By gently loading a biological small-molecule solution at the bottom of a cuvette preloaded with non-selective Mueller-Hinton culture medium, we were able to record the maximum absorbance wavelength of the small-molecule as it diffused up in solution along the cuvette height (Fig. 3d, Fig. S15). This allowed us to easily correlate the small molecule's diffusion with its absorbance as it moves upward along the cuvette (mimicking the small molecule diffusion along the side-channels). To test the validity of this methodology for determining the mass transport of small-molecules, we picked three antibiotics as biological small-molecules (nalidixic acid, cefuroxime, and ampicillin) in addition to resazurin. Our results indicated that the small-molecules with similar molar volumes (*e.g.*, resazurin/nalidixic acid and cefuroxime/ampicillin) show very close absorbance curves over time (i.e., similar diffusion patterns in the cuvette solution; Fig. 3e). This confirms that the easily-found molar volume of a small-molecule can be used to calculate the appropriate loading time in our device based on Equation-1, rather than relying on the more difficult-to-determine diffusion coefficient. Based on this methodology, we list the loading times of most commercial antibiotics, antifungal, and anticancer drugs (Supplementary Tables 1–3), potentially allowing this platform to be employed for further studies.

3.4. MVM^2 platform testing for eukaryotic and prokaryotic cells

In terms of practical application of the MVM^2 platform for different biological assays, we note that water evaporation can become an issue for nanoliter-sized culture media in the microchambers due to the permeability of the PDMS walls (Fig. S16). This can lead to small-molecule concentration changes, particularly for long-term biological assay measurements. To overcome this issue, we have considered a water bath design in our MVM^2 platform to obtain evaporative equilibrium (Fig. S17). The simple design improves the device's capability to run long-term biological assays, such as cancer cell-anticancer drug testing (*e.g.*, >24 h), as well as relatively short-term ones, such as bacteria-antibiotic testing (*e.g.*, <8 h; Fig. S18).

To further examine the functionality of our MVM^2 platform and due to the importance of worldwide emerging resistance to antibacterial drugs, we studied the susceptibility of a green fluorescent protein (GFP)-labeled *E. coli* 541–15 to gentamicin (a typical antibiotic) in order to determine the minimum inhibitory concentration (MIC) of the antibiotic. We first loaded the *E. coli* 541-15 bacterial suspension (concentration:1×10^6 CFU/mL) into the microchambers (step i). Resazurin (5 wt%) was also added to the bacterial suspension to allow us to monitor the bacterial cell metabolism through an irreversible resazurin-resorufin enzymatic reduction reaction (*i.e.*, with increasing bacterial growth, the higher resazurin reduction results in greater fluorescent intensity). We then generated a GCP of the gentamicin (loading time = 170 s; Table 1) in the positive microchambers (step-ii) in the concentration range of 0.1–100 μg/mL, specifically 0.1–1 (low), 1–10 (medium), and 10–100 (high) μg/mL for the three channels. At t = 0 h, the negative and positive microchambers feature the same low red fluorescent intensities of resazurin, as expected (Fig. S19). After incubation of the bacteria for 4 h at 37 °C, the red fluorescent intensities of all the negative controls (*i.e.*, no gentamicin exposure) increased, indicating bacterial growth (Fig. 4a). Additionally, we obtained fluorescent intensities as high as the negative controls for positive microchambers R_9–R_{12}, suggesting the antibiotic concentration in these microchambers was not sufficient to retard/stop the bacterial growth. Meanwhile, the other positive microchambers (R_1–R_8, gentamicin concentration C_1–C_8 > C_9–C_{12}) showed relatively lower fluorescent intensity. These results clearly indicated the MIC at which the *E. coli* 541–15 was susceptible to the gentamicin.

To further confirm these findings based on the bacterial cell metabolism obtained from resazurin reduction, we correlated the red fluorescent intensities with the green fluorescence directly associated with the GFP-labeled bacterial growth in the corresponding microchambers (Fig. 4a and b). Both red and green fluorescent modes confirmed excellent correlation between the bacterial growth and resazurin reduction. By converting the red fluorescent intensities to gray values, we calculated 2.82 ± 0.68 μg/mL (n = 5) as the MIC of gentamicin (Fig. 4c and d). Moreover, we used the gold standard broth microdilution technique (measuring the bacterial cell density—OD_{600}—*vs.* the incubation time) to validate the MVM^2 platform functionality (Fig. 4e). We obtained 3 ± 2 μg/mL (n = 5) as the MIC for the *E. coli* 541–15/gentamicin pair, which is in excellent agreement with the MVM^2 finding.

As a representative small-molecule model (assay), showing a bacterial resistance to antibiotics, we also examined the ampicillin-*E. coli* 541-15 pair assay. Similarly, we probed the bacterial cell metabolism and growth using the resazurin reduction assay and monitored changes in the number of GFP-labeled bacteria during the assay, as shown in Figs. S20 and S21, respectively. There was no significant difference in the red or green fluorescent intensities of the negative control (0 μg/mL) and high range (10–100 μg/mL)—confirming the bacterial resistance to ampicillin. Note, the data for the low and medium ranges are not shown in Figs. S20 and S21, respectively. Moreover, we also used the broth microdilution assay to confirm this finding for the *E. coli* 541-15-ampicillin pair in the MVM^2 platform, which also showed the resistance of *E. coli* 541–15 to ampicillin (Fig. S22).

To further evaluate our platform functionality, we tested isolated bacteria from two clinical scenarios ((i) ileal mucosa of human patients associated with Crohn's disease in Fig. 4f and (ii) bovine mastitis in Fig. S23) *vs.* relevant antibiotics, testing the most important mechanisms of action for antibiotics. Fig. 4f and Fig. S23 consist of the following information: (i) The type of bacteria and tested antibiotic can be found at the left and right sides, respectively. (ii) Each row includes 37 squares, as labeled at the top and have been categorized in 4 different categories—first square representing the microchamber as negative control (labeled with "N"), and every next twelve squares as respectively representing low, medium, and high positive ranges of antibiotic concentrations. (iii) The low, medium, and high ranges are included the concentration ranges of 0.1–1, 1–10, and 10–100 μg/mL (iii) There are three types of squares: dark red, dark pink or light pink. If bacteria is susceptible to a specific antibiotic (*e.g.*, *E. coli* LF82/gentamicin pair in Fig. 4f), below MIC (shown by dark pink color), bacteria can survive and grow causing more resazurin reduction (shown by dark red). Over than MIC, the bacterial growth stopped as shown by light pink color. The dark pink squares also show the microchambers which antimicrobial susceptibility was monitored at different trials. As bacteria resistance to antibiotic (*e.g.*, *E. coli* LF82/ampicillin pair in Fig. 4f), then all microchambers are dark red demonstrating the well-grown bacteria in the presence of the tested antibiotic in microchambers. For ileal mucosa of human patients associated with Crohn's disease (Fig. 4f), the most effective antibiotic was gentamicin, effective through inhibiting protein synthesis by targeting 30S subunit of ribosome.

To probe the functionality of our MVM^2 platform for eukaryotic cells, we first showed its long-term cell-culture and growth capability for cancer and yeast cells (the MCF-7 human breast cancer cell line and a *Saccharomyces cerevisiae* strain, respectively) in Figs. S24 and S25. Then, as an example, we chose to use the platform to study recessive human metabolic diseases, specifically measuring sugar-phosphate toxicity. For these experiments, we chose a strain of *S. cerevisiae* in which fructose, but not glucose, is toxic due to constitutive expression of a rat liver ketohexokinase gene (the yrKHK strain, DBY12549). The data obtained using the MVM^2 platform precisely pinpointed the binary 'Yes/No' sensitivity response of the yrKHK strain to fructose (Yes) and glucose (No), as shown in Figs. S26 and S27, respectively. Moreover, a fructose

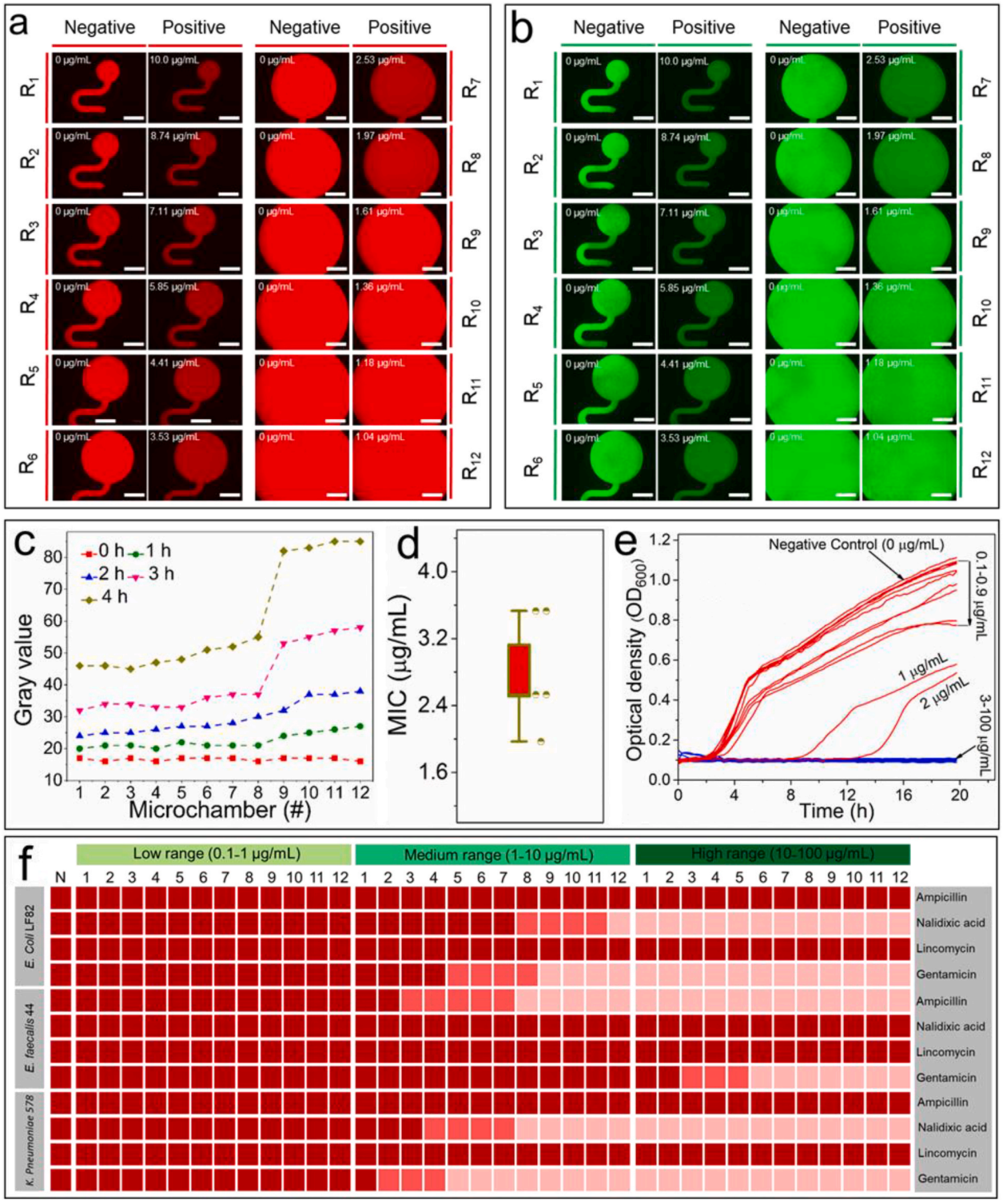

Fig. 4. Functionality of the MVM^2 platform. The antimicrobial susceptibility assay for *E. coli* 541–15 as a bacteria species susceptible to gentamicin after incubation for 4 h in: (a) red fluorescent mode (representing resazurin reduction correlated with bacterial metabolites) and (b) green fluorescent modes (visualizing the GFP-labeled bacterial growth/inhibition). We used kanamycin at an appropriate concentration (50 μg/mL) in the bacteria/resazurin suspension, avoiding bacteria-inserted GFP plasmid repulsion during the antimicrobial resistant assay. (c) Gray values for the positive microchambers in the medium range (1–10 μg/mL) over 4-h antimicrobial susceptibility testing. The gray values were obtained by converting the fluorescent intensity produced from resazurin-reduction in the culture medium, which correlates with the *E. coli* 541-15 bacterial growth. (d) Determining the MIC of the *E. coli* 541–15/gentamicin pair. (e) Validation of the MVM^2 platform functionality using the gold standard broth microdilution technique. (f) Crohn's diseases' clinically isolated *E. coli* LF82, *E. faecalis* 44, and *K. pneumoniae* 578 tested *via* four clinically relevant antibiotics including: ampicillin, nalidixic acid, lincomycin, and gentamicin. Scale-bar in (a) and (b): 200 μm. (For interpretation of the references to color in this figure legend, the reader is referred to the Web version of this article.)

concentration of 1.13 wt% was determined as the critical sensitivity concentration for the yrKHK strain using the MVM^2 platform (Figs. S26 and S27), which is in excellent agreement with the analogous growth curves (Fig. S27). Finally, we also studied the resistant outcome of a wild-type *S. cerevisiae* strain (DBY12000) to fructose and glucose, in which the wild-type *S. cerevisiae* growth continued regardless of the sugar concentrations as expected (Figs. S28 and S29).

4. Conclusion

In summary, compared with previous milestones in developing microfluidic platforms for biological assays, this is to the best of our knowledge the first microfluidics device that is able to: (i) test small-molecules on both eukaryotic and prokaryotic cells; (ii) work in a high-throughput mode with an extended range of small-molecule concentrations (*e.g.*, three orders of magnitude), while also including negative controls; (iii) exploit a low-cost microfluidics chip (~$1 each) using a facile operation protocol; and (iv) prepare the desired sample concentrations very precisely using fluid dynamics with minimal human intervention. Moreover, future integration of this platform with other technologies, such as complementary metal oxide semiconductor imaging, or electrochemical responses, could readily pave the way to employ this platform for numerous biological assays, such as cancer cell biology, cell signaling, protein/small-molecule interactions, pesticide analysis, *etc.* Building from this MVM^2 concept, we envision further advanced platforms made possible by the easily modified MVM^2 features, which could be applied to even broader future biological and non-biological analytical applications.

CRediT authorship contribution statement

Morteza Azizi: Formal analysis, Writing – original draft, designed research, performed the experiments and analyzed the data. All authors have contributions in writing the manuscript. **Ann V. Nguyen:** Formal analysis, Writing – original draft, performed the experiments and analyzed the data. All authors have contributions in writing the manuscript. **Amir Mokhtare:** Formal analysis, Writing – original draft, performed the experiments and analyzed the data. All authors have contributions in writing the manuscript. **Shiying Zhang:** Formal analysis, Writing – original draft, performed the experiments and analyzed the data. All authors have contributions in writing the manuscript. **Belgin Dogan:** Writing – original draft, performed the experiments and analyzed the data. All authors have contributions in writing the manuscript. **Patrick A. Gibney:** Writing – original draft, designed research. **Kenneth W. Simpson:** Writing – original draft, designed research. **Alireza Abbaspourrad:** Writing – original draft, designed research.

Declaration of competing interest

The authors declare that they have no known competing financial interests or personal relationships that could have appeared to influence the work reported in this paper.

Acknowledgments

This work was performed in part at the Cornell NanoScale Facility, a member of the National Nanotechnology Coordinated Infrastructure (NNCI), which is supported by the National Science Foundation (Grant NNCI-2025233).

Appendix A. Supplementary data

Supplementary data to this article can be found online at https://doi.org/10.1016/j.bios.2021.113038.

References

Alsenaid, A., Ezmerli, M., Srour, J., Heppt, M., Illigens, B.M., Prinz, J.C., 2020. J. Dermatol. Treat. 1–10.
and, Y.X., Whitesides, G.M., 1998. Annu. Rev. Mater. Sci. 28 (1), 153–184.
Avesar, J., Rosenfeld, D., Truman-Rosentsvit, M., Ben-Arye, T., Geffen, Y., Bercovici, M., Levenberg, S., 2017. Proc. Natl. Acad. Sci. Unit. States Am. 114 (29), E5787–E5795.
Azizi, M., Zaferani, M., Dogan, B., Zhang, S., Simpson, K.W., Abbaspourrad, A., 2018. Anal. Chem. 90 (24), 14137–14144.
Baltekin, Ö., Boucharin, A., Tano, E., Andersson, D.I., Elf, J., 2017. Proc. Natl. Acad. Sci. Unit. States Am. 114 (34), 9170–9175.
Campbell, J., McBeth, C., Kalashnikov, M., Boardman, A.K., Sharon, A., Sauer-Budge, A. F., 2016. Biomed. Microdevices 18 (6), 103.
Gibney, P.A., Schieler, A., Chen, J.C., Bacha-Hummel, J.M., Botstein, M., Volpe, M., Silverman, S.J., Xu, Y., Bennett, B.D., Rabinowitz, J.D., Botstein, D., 2018. Mol. Biol. Cell 29 (8), 897–910.
Hong, W., Karanja, C.W., Abutaleb, N.S., Younis, W., Zhang, X., Seleem, M.N., Cheng, J.-X., 2018. Anal. Chem. 90 (6), 3737–3743.
Huang, X., Xu, D., Chen, J., Liu, J., Li, Y., Song, J., Ma, X., Guo, J., 2018. Analyst 143 (22), 5339–5351.
Jang, Y.-H., Hancock, M.J., Kim, S.B., Selimović, Š., Sim, W.Y., Bae, H., Khademhosseini, A., 2011. Lab Chip 11 (19), 3277–3286.
Johnston, N.R., Strobel, S.A., 2019. Chem. Res. Toxicol. 32 (11), 2305–2319.
Kao, Y.-T., Kaminski, T.S., Postek, W., Guzowski, J., Makuch, K., Ruszczak, A., von Stetten, F., Zengerle, R., Garstecki, P., 2020. Lab Chip 20 (1), 54–63.
Kim, J., Taylor, D., Agrawal, N., Wang, H., Kim, H., Han, A., Rege, K., Jayaraman, A., 2012. Lab Chip 12 (10), 1813–1822.
Kim, S., Masum, F., Jeon, J.S., 2019. BioChip Journal 13 (1), 43–52.
Lamb, J., Crawford, E.D., Peck, D., Modell, J.W., Blat, I.C., Wrobel, M.J., Lerner, J., Brunet, J.-P., Subramanian, A., Ross, K.N., 2006. Science 313 (5795), 1929–1935.
Leonard, H., Halachmi, S., Ben-Dov, N., Nativ, O., Segal, E., 2017. ACS Nano 11 (6), 6167–6177.
Li, H., Torab, P., Mach, K.E., Surrette, C., England, M.R., Craft, D.W., Thomas, N.J., Liao, J.C., Puleo, C., Wong, P.K., 2019. Proc. Natl. Acad. Sci. Unit. States Am. 116 (21), 10270–10279.
Lim, W., Park, S., 2018. Molecules 23 (12), 3355.
Liu, J., Geng, Z., Fan, Z., Liu, J., Chen, H., 2019. Biosens. Bioelectron. 132, 17–37.
Machado, C.M., De-Souza, E.A., De-Queiroz, A.L.F.V., Pimentel, F.S.A., Silva, G.F.S., Gomes, F.M., Montero-Lomelí, M., Masuda, C.A., 2017. Molecular Basis of Disease 1863 (6), 1403–1409.
Mohan, R., Mukherjee, A., Sevgen, S.E., Sanpitakseree, C., Lee, J., Schroeder, C.M., Kenis, P.J.A., 2013. Biosens. Bioelectron. 49, 118–125.
Mosquera, J., García, I., Liz-Marzán, L.M., 2018. Accounts of Chemical Research 51 (9), 2305–2313.
Pajoumshariati, S.R., Azizi, M., Wesner, D., Miller, P.G., Shuler, M.L., Abbaspourrad, A., 2018a. ACS Appl. Mater. Interfaces 10 (11), 9235–9246.
Pajoumshariati, S.R., Azizi, M., Zhang, S., Dogan, B., Simpson, K.W., Abbaspourrad, A., 2018b. Adv. Funct. Mater. 28 (48), 1805568.
Reddy, B., Hassan, U., Seymour, C., Angus, D.C., Isbell, T.S., White, K., Weir, W., Yeh, L., Vincent, A., Bashir, R., 2018. Nature Biomedical Engineering 2 (9), 640–648.
Sarzi-Puttini, P., Ceribelli, A., Marotto, D., Batticciotto, A., Atzeni, F., 2019. Autoimmun. Rev. 18 (6), 583–592.
Stockwell, B.R., 2004. Nature 432 (7019), 846–854.
Syal, K., Iriya, R., Yang, Y., Yu, H., Wang, S., Haydel, S.E., Chen, H.-Y., Tao, N., 2016. ACS Nano 10 (1), 845–852.
Wikler, M.A., Cockerill, F.R., Bush, K., Dudley, M.N., Elipoulos, G.M., Hardy, D.J., Hecht, D.W., Hindler, J.F., Patel, J.B., Powell, M., Turnidge, J.D., Weinstein, M.P., Zimmer, B.L., Ferraro, M.J., Swenson, J.M., 2012. Standard M07-A9, vol. 32, 2.
Wootton, R.C.R., deMello, A.J., 2012. Nature 483 (7387), 43–44.
Xu, D., Huang, X., Guo, J., Ma, X., 2018a. Biosens. Bioelectron. 110, 78–88.
Xu, Y.-F., Lu, W., Chen, J.C., Johnson, S.A., Gibney, P.A., Thomas, D.G., Brown, G., May, A.L., Campagna, S.R., Yakunin, A.F., Botstein, D., Rabinowitz, J.D., 2018b. ACS Chem. Biol. 13 (10), 3011–3020.
Yaghoobi, M., Azizi, M., Mokhtare, A., Abbaspourrad, A., 2020. BioRxiv. https://doi.org/10.1101/2020.07.31.231373.
Yang, Y., Gupta, K., Ekinci, K.L., 2020. Proc. Natl. Acad. Sci. Unit. States Am. 117 (20), 10639–10644.